

# Tidal-locking-induced stellar rotation dichotomy in the open cluster NGC 2287?

WEIJIA SUN,<sup>1,2</sup> CHENGYUAN LI,<sup>3,2</sup> LICAI DENG,<sup>2,4,5</sup> AND RICHARD DE GRIJS<sup>6,7,8</sup>

<sup>1</sup>*Kavli Institute for Astronomy & Astrophysics and Department of Astronomy, Peking University, Yi He Yuan Lu 5, Hai Dian District, Beijing 100871, China*

<sup>2</sup>*Key Laboratory for Optical Astronomy, National Astronomical Observatories, Chinese Academy of Sciences, 20A Datun Road, Chaoyang District, Beijing 100012, China*

<sup>3</sup>*School of Physics and Astronomy, Sun Yat-sen University, Zhuhai 519082, China*

<sup>4</sup>*School of Astronomy and Space Science, University of the Chinese Academy of Sciences, Huairou 101408, China*

<sup>5</sup>*Department of Astronomy, China West Normal University, Nanchong 637002, China*

<sup>6</sup>*Department of Physics and Astronomy, Macquarie University, Balacava Road, Sydney, NSW 2109, Australia*

<sup>7</sup>*Research Centre for Astronomy, Astrophysics and Astrophotonics, Macquarie University, Balacava Road, Sydney, NSW 2109, Australia*

<sup>8</sup>*International Space Science Institute–Beijing, 1 Nanertiao, Hai Dian District, Beijing 100190, China*

## ABSTRACT

Stars spend most of their lifetimes on the ‘main sequence’ (MS) in the Hertzsprung–Russell diagram. The obvious double MSs seen in the equivalent color–magnitude diagrams characteristic of Milky Way open clusters pose a fundamental challenge to our traditional understanding of star clusters as ‘single stellar populations.’ The clear MS bifurcation of early-type stars with masses greater than  $\sim 1.6 M_{\odot}$  is thought to result from a range in the stellar rotation rates. However, direct evidence connecting double MSs to stellar rotation properties has yet to emerge. Here, we show through analysis of the projected stellar rotational velocities ( $v \sin i$ , where  $i$  represents the star’s inclination angle) that the well-separated double MS in the young,  $\sim 200$  Myr-old Milky Way open cluster NGC 2287 is tightly correlated with a dichotomous distribution of stellar rotation rates. We discuss whether our observations may reflect the effects of tidal locking affecting a fraction of the cluster’s member stars in stellar binary systems. We show that the slow rotators could potentially be initially rapidly rotating stars that have been slowed down by tidal locking by a low mass-ratio companion in a cluster containing a large fraction of short-period, low-mass-ratio binaries. This demonstrates that stellar rotation drives the split MSs in young,  $\lesssim 300$  Myr-old star clusters. However, special conditions, e.g., as regards the mass-ratio distribution, might be required for this scenario to hold.

**Keywords:** stars: rotation — open clusters and associations: individual: NGC 2287 — galaxies: star clusters: general.

## 1. INTRODUCTION

Over the last decade, multiple studies have revealed the common occurrence of bifurcated main sequences (MSs) in young,  $\leq 400$  Myr-old star clusters in the Large and Small Magellanic Clouds (LMC and SMC; Milone et al. 2015; D’Antona et al. 2015; Milone et al. 2016, 2017; Li et al. 2017; Correnti et al. 2017; Milone et al. 2018). A split MS was first observed in NGC 1844 by Milone et al. (2013). Combined with extended MS turn-off regions (eMSTOs), which have been discovered in intermediate-age,  $\leq 3$  Gyr-old LMC and SMC clusters (e.g. Mackey et al. 2008; Milone et al. 2009; Goudfrooij et al. 2011), these split MSs pose a fundamental challenge to our traditional understanding of star clusters as prototypes of the canonical ‘simple’ stellar population.

Unlike the multiple MSs found in globular clusters, which are owing to variations in helium abundance (for a review, see Bastian & Lardo 2018), the split MSs in young clusters are believed to have an alternative origin (Milone et al. 2015). Based on a comparison of the clusters’ color–magnitude diagrams (CMDs) with stellar evolutionary models, D’Antona et al. (2015); Milone et al. (2016) suggested that the observed split MSs are consistent with two coeval populations characterized by different rotation rates: a non-rotating population of blue MS (bMS) stars and a rapidly rotating population of red MS (rMS) stars. The presence of a large fraction of fast rotators in these clusters was first confirmed by employing Be stars (rapidly rotating B-type stars exhibiting H $\alpha$  emission Rivinius et al. 2013) as probes.

Using  $H\alpha$  images observed with the *Hubble Space Telescope* (*HST*), Bastian et al. (2017); Milone et al. (2018) searched for Be stars in young, massive LMC clusters. They confirmed that Be stars populate the rMS and the reddest part of the eMSTO. Spectroscopic evidence directly confirming the stellar rotation properties was subsequently provided by Dupree et al. (2017); Marino et al. (2018b), supporting this rotation-dominant picture.

Based on the *Gaia* Data Release 2 (DR2; Gaia Collaboration et al. 2016, 2018), Cordoni et al. (2018) found that eMSTOs are a common feature in young and intermediate-age clusters in the Milky Way and that they may be governed by a similar mechanism as in Magellanic Clouds. The presence of stars with rotation rates ranging from slow to nearly critical rotation has been reported based on observations of field stars and open clusters (Huang & Gies 2006; Huang et al. 2010), and the effects of stellar rotation in the MSTO region have also been studied (Brandt & Huang 2015c,a,b). However, a direct connection between stellar rotation and the presence of a split MS/eMSTO has only been established for a limited number of clusters. Bastian et al. (2018), Marino et al. (2018a), and Sun et al. (2019) measured the rotational velocities of MS stars in three Galactic open clusters (OCs) and confirmed the presence of populations with different rotation rates.

In this paper, we analyze the Galactic OC NGC 2287, which shows a clearly split MS following stellar membership selection based on *Gaia* DR2 (Cordoni et al. 2018). We verify that the split MS is a genuine characteristic and not caused by differential extinction. The bMS and rMS are well separated in projected rotational velocity  $v \sin i$ , in the sense that bMS stars are composed of slow rotators and rMS stars are mainly rapid rotators. MSTO stars also show a similar correlation between their colors and the projected rotational velocities. Our results suggest that they follow a dichotomous distribution in equatorial rotational velocity. To interpret our results, the scenario proposed by D’Antona et al. (2017), which suggests that slowly rotating stars could have been initially rapidly rotating stars that have been slowed down by tidal locking by a low mass-ratio companion, is not ruled out. However, these binaries may, in fact, be subject to special conditions in terms of their period and mass-ratio distributions.

This article is organized as follows. We present the membership determination, spectroscopic data, and stellar classification in Section 2. In Section 3 we analyze the stellar rotation rates in the split MS and MSTO regions. Our discussion and conclusions are covered in Section 4.

## 2. DATA AND ANALYSIS

### 2.1. Membership determination

From *Gaia* DR2, we obtained the photometric measurements and derived the membership probabilities of the NGC 2287 cluster stars based on their proper motions and parallaxes. We searched for all stars within  $2^\circ$  of the center of NGC 2287 in the *Gaia* DR2 database. In the vector-point diagram of its stellar proper motions (see the left panel of Fig. 1), NGC 2287 is well separated and concentrated at  $(\mu_\alpha \cos \theta, \mu_\delta) \approx (-4.34, -1.37) \text{ mas yr}^{-1}$ . We defined  $\mu_R = \sqrt{(\mu_\alpha \cos \theta - \langle \mu_\alpha \cos \theta \rangle)^2 + (\mu_\delta - \langle \mu_\delta \rangle)^2}$  and used  $\mu_R \leq 0.6 \text{ mas yr}^{-1}$  as our primary selection criterion. Next, we calculated the median value of  $\varpi$  and the corresponding r.m.s. ( $\sigma$ ) for stars clustered near  $\varpi \sim 1.4 \text{ mas yr}^{-1}$ . These stars were further selected based on their parallax measurements, within  $2\sigma$ , i.e.,  $1.2215 \text{ mas yr}^{-1} \leq \varpi \leq 1.5060 \text{ mas yr}^{-1}$  (see the red dashed lines in the middle panel of Fig. 1, corresponding to distances between 818 pc and 664 pc). The *Gaia*-based CMD of the cluster’s member stars, combined with that of all stars in the field, is presented in the right panel of Fig. 1. NGC 2287 shows multiple clearly defined MSs at  $G$  band magnitudes from 10.5 mag to 11.5 mag. A binary sequence above the MS is clearly visible.

### 2.2. Spectroscopic data

For NGC 2287, high-resolution spectra were obtained with the European Southern Observatory’s Very Large Telescope equipped with the FLAMES/GIRAFFE spectrograph (Pasquini et al. 2002), collected as part of programs 380.D-0161(A) and 380.D-0161(B) (PI Gieles). The HR14B spectral setup employed offers a nominal resolution of  $R \approx \lambda/\Delta\lambda \approx 29,000$ , covering wavelengths from 5139 Å to 5356 Å. We retrieved wavelength-calibrated spectra from the ESO archive, which had been reduced by the GIRAFFE pipeline. In total, 166 member stars were observed as part of these programs. In this paper, we study 53 bright stars covering the eMSTO, rMS, bMS, and the equal-mass binary sequence (see Section 2.4 and Fig. 3). The typical signal-to-noise ratio of the spectra is  $\sim 100$ . Most of the bright member stars were observed twice within 3 months.

### 2.3. Isochrone fitting

In Fig. 2, a set of isochrones from PARSEC 1.2S (Bressan et al. 2012) for solar metallicity  $Z = 0.0152$  and extinction  $A_V = 0.217 \text{ mag}$  is overplotted. The extinction coefficients for the *Gaia* bands were estimated based on the Cardelli

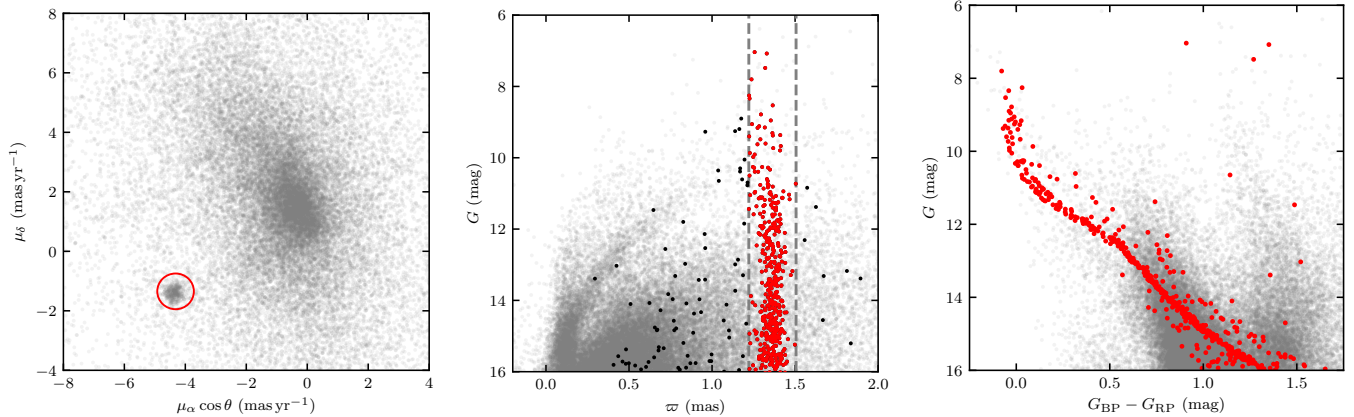


**Figure 1.** (left) Vector-point diagram of the proper motions of stars brighter than  $G = 16$  mag located within  $2^\circ$  of the NGC 2287 center. The red circle shows the primary selection area ( $0.6 \text{ mas yr}^{-1}$ ). (middle)  $G$ -band photometry versus stellar parallaxes. The parallax-selected members are marked as red dots. The vertical dashed lines represent the parallax selection boundaries. (right) CMD of all stars in the field (grey dots) and the NGC 2287 member stars (red solid dots). A split MS is visible around  $G \sim 11$  mag.

et al. (1989) and O'Donnell (1994) extinction curve with  $R_V = 3.1$ . The corresponding ages range from 150 Myr to 350 Myr in steps of 50 Myr, covering the blue and red ridge lines of the split MS. We performed our CMD fitting based on visual matching. The best-fitting isochrone to the blue edge of the bulk stellar population has an age of 150 Myr and a distance modulus of 9.33 ( $\sim 734$  pc).

Platais et al. (2012) suggested that differential extinction could generate an artificial eMSTO. However, it is unlikely that the split MS phenomenon we observe in NGC 2287 is somehow produced by differential extinction. To prove that the effect of differential extinction is negligible, we inspected the width of the MS (see the dashed box in Fig. 2). In the inset, we show the best-fitting isochrone (red solid line) as well as that same isochrone shifted by 0.02 mag in color (red dashed lines). We found that most MS stars are encompassed within the dashed lines, indicating very limited differential extinction. The clearly isolated equal-mass binary sequence also suggests that differential reddening is negligible.

#### 2.4. Classification

Fig. 3 shows the CMD pertaining to the cluster's member stars, in *Gaia* passbands. We classified the member stars into four groups on the basis on their loci in the CMD: eMSTO (green squares), bMS (blue triangles), rMS (red circles), and equal-mass binary systems (yellow diamonds). Stars brighter than the bulk MS population by 0.75 mag were identified as equal-mass binary stars. Other stars brighter than  $G \sim 10$  mag were classified as eMSTO stars, whereas the fainter stars were assigned to the bMS and rMS according to their colors. At the faint end, around  $G \sim 12$  mag, the split MSs converge. We did not include these stars in our analysis. The number of stars with available spectroscopic data account for half the population in each group, and therefore we estimated that the completeness levels for all groups is around 50–60%.

The MS region is composed of three components, including two well-separated MSs and a sparse sequence populated by equal-mass binary systems. The (leftmost) bMS can be adequately approximated by a single-star isochrone, while the parallel and slightly offset rMS is also well-defined. The discrete nature of the rMS and bMS in the CMD renders this cluster of particular interest in the context of previous studies of young clusters, where the target objects were too distant to perform reliable stellar membership determinations (Marino et al. 2018b) or where the MS region was smeared out (Marino et al. 2018a).

We found seven spectroscopic binary candidates in our sample. Only one is classified as a single-lined spectroscopic binary. Its absorption lines show a significant shift in radial velocity ( $\sim 50 \text{ km s}^{-1}$ ) between two observational visits. The others are classified as double-lined spectroscopic binaries. The relevant finding chart did not reveal any suitable companion stars within 2.0 arcsec (1.2 arcsec fiber diameter plus 0.8 arcsec seeing) for these candidates. Most of these

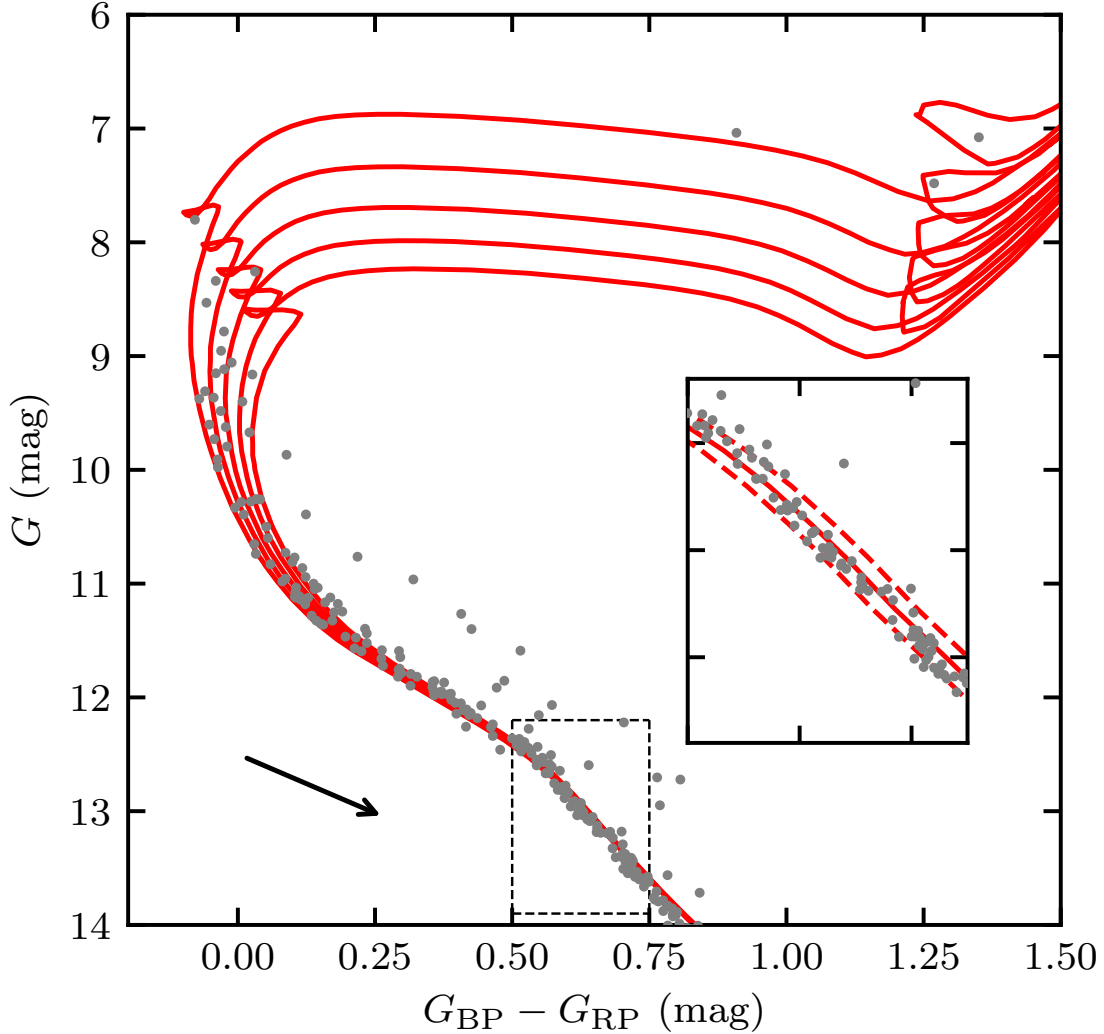


**Figure 2.** CMD of the OC NGC 2287 in the *Gaia* passbands. Grey dots represent all stars in the cluster field. Black dots represent cluster member stars selected based on *Gaia* DR2. The best-fitting (leftmost) PARSEC isochrone (Bressan et al. 2012) to the bluest edge of the bulk stellar population has an age of 150 Myr, a metallicity  $Z = 0.0152$ , and a distance of  $\sim 734$  pc. Isochrones for ages from 150 Myr to 350 Myr (in steps of 50 Myr) are also overplotted. The black arrow indicates the direction of the reddening vector. The dashed box is shown in more detail in the inset, where the solid line is the best-fitting isochrone and the dashed lines show the same isochrone shifted by 0.02 mag in color.

binaries exhibit relatively narrow absorption profiles, except for *Gaia* ID 2927014822050825856. The latter has a relatively broad absorption profile accompanied by a second sharp and narrow absorption line in its center. This additional absorption feature is only present at wavelengths around 5167 Å. We confirmed that this feature remained unchanged between two observations separated by 78 days. Since there is no other source discernible close to this candidate star, the additional absorption in the core of its broad absorption profile might come from an unresolved binary system including a secondary star with a low effective temperature but a rather high metallicity. Such a companion can form a narrow MgI triplet line without affecting the other components (e.g., the continuum) of the spectrum. We did not attempt to estimate its  $v \sin i$ , because the spectrum cannot be well fitted by a rotationally broadened profile (see Table 1).

### 3. STELLAR ROTATION

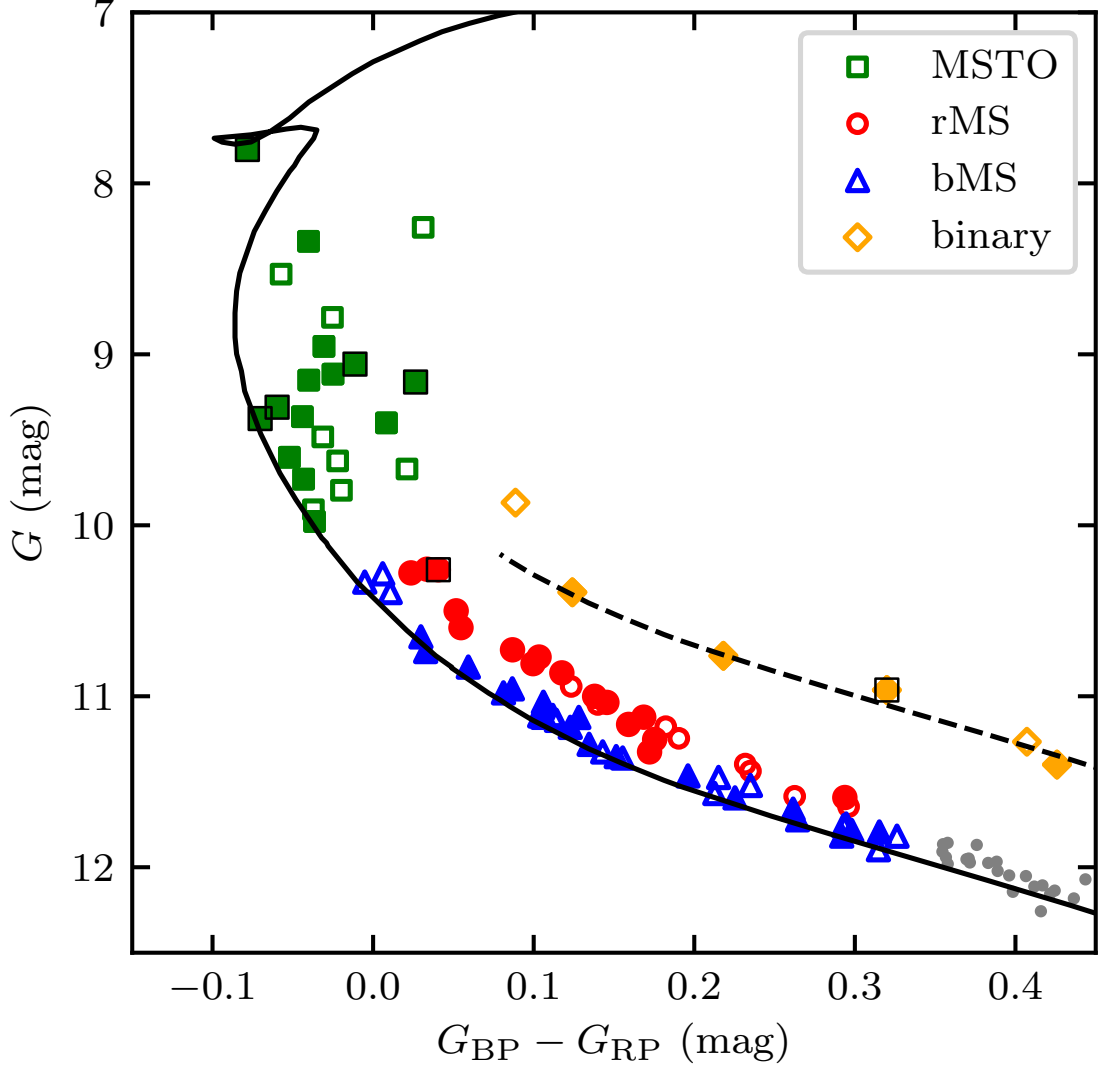


**Figure 3.** CMD of the OC NGC 2287 around its eMSTO and split-MS regions. bMS, rMS, MSTO, and binary stars are represented by blue triangles, red circles, green squares, and yellow diamonds, respectively. Spectroscopically analyzed stars are marked with solid markers. The black solid and dashed lines represent the best-fitting PARSEC isochrone (Bressan et al. 2012) and the corresponding equal-mass binary sequence, respectively. Squares represent spectroscopic binaries.

We used the absorption-line profiles of the Mgi triplet to calculate the projected rotational velocities. We first derived synthetic stellar spectra from the Pollux database (Palacios et al. 2010) with effective temperatures ( $T_{\text{eff}}$ ) from 6400 K to 11000 K (using steps of 100 K), surface gravities from  $\log g = 3.5$  to  $\log g = 5.0$  (steps of 0.5) and metallicity from  $[\text{Fe}/\text{H}] = -1.0$  dex to  $[\text{Fe}/\text{H}] = 1.0$  dex (steps of 0.5 dex). The spectra were then computed based on the plane-parallel ATLAS12 model atmospheres in local thermodynamic equilibrium (Kurucz 2005). The microturbulent velocity was fixed at  $2 \text{ km s}^{-1}$  for all models. Synthetic spectra were then generated using the SYNSPEC tool (Hubeny & Lanz 1992). A Gaussian kernel of  $\sigma = 0.075 \text{ \AA}$  (corresponding to a spectral resolution of 29,000 at  $5100 \text{ \AA}$ ) was applied to the model spectra to represent the effects of instrumental broadening. Next, they were convolved with a rotational  $v \sin i$  profile from  $5 \text{ km s}^{-1}$  to  $400 \text{ km s}^{-1}$  (steps of  $5 \text{ km s}^{-1}$ ) and shifted by a radial velocity from  $0 \text{ km s}^{-1}$  to  $50 \text{ km s}^{-1}$  in steps of  $2 \text{ km s}^{-1}$  (the average radial velocity is  $23.3 \text{ km s}^{-1}$ ; Kharchenko et al. 2005). Finally, the model spectra were resampled to match the observed spectra using  $\chi^2$  minimization.

Since no Balmer lines are covered by the observed wavelength range, it is hard to determine a reliable effective temperature. Therefore, we adopted the measured  $T_{\text{eff}}$  from *Gaia* DR2 as our initial guess for each individual spectrum

and searched for the best model with an effective temperature within 500 K of the initial value. Although the *Gaia* DR2  $T_{\text{eff}}$  values have not been corrected for extinction (Andrae et al. 2018), this is nevertheless a generally acceptable practice. On the one hand, the extinction to NGC 2287 ( $A_V = 0.217$  mag) is smaller than the median extinction value (0.335 mag) of the low-extinction data set used to estimate the effective temperatures (Andrae et al. 2018), thus allowing us to infer reliable effective temperatures of this cluster’s member stars using  $T_{\text{eff}}$  values from *Gaia* DR2. On the other hand, we have also adopted a 500 K buffer area to avoid any systematic differences from the actual values. The projected rotational velocity is weakly dependent on some stellar parameters. We estimated the uncertainty in  $v \sin i$  by remeasuring mock spectra generated from the model template with different signal-to-noise ratios. This procedure was repeated 100 times and the 68th percentile of the projected rotational velocity distribution was taken as the uncertainty. The minimum value of the uncertainty was fixed at  $5 \text{ km s}^{-1}$ , reflecting the limitation owing to the grid’s step sizes. As for stars with multiple observations, we confirmed that there were no significant variations in their stellar parameters, including in their radial and projected rotational velocities (exceptions were discussed in the previous section) between each visit. The typical difference is within the prevailing uncertainties. The inferred  $v \sin i$  values are listed in Table 1.

**Table 1.** Projected rotational velocities of member stars in NGC 2287.

<i>Gaia</i> ID	$G$ (mag)	$G_{\text{bp}}$ (mag)	$G_{\text{rp}}$ (mag)	$\Delta G_{\text{BP}} - G_{\text{RP}}$	$v \sin i$ ( $\text{km s}^{-1}$ ) <sup>a</sup>	Classification
(1)	(2)	(3)	(4)	(5)	(6)	(7)
2927207133504349056	11.47	11.53	11.34	0.02	$70 \pm 9$	bMS
2926993995745289216	11.66	11.75	11.49	0.03	$80 \pm 14$	bMS
2926994103128768768	11.79	11.91	11.59	0.03	$50 \pm 15$	bMS
2926990048679648000	11.79	11.89	11.59	0.02	$85 \pm 15$	bMS
2927014787691101696	11.28	11.33	11.19	0.01	$120 \pm 12$	bMS
2927008224981157760	10.83	10.85	10.79	0.01	$60 \pm 13$	bMS
2927199505642285824	11.59	11.67	11.45	0.01	$85 \pm 11$	bMS
2927007262908564736	11.12	11.16	11.06	0.01	$125 \pm 10$	bMS
2927204517860633344	10.98	11.02	10.94	0.01	$130 \pm 8$	bMS
2926995030833789056	11.35	11.40	11.25	0.01	$105 \pm 13$	bMS
2927002040228145280	10.96	10.99	10.90	0.02	$172 \pm 10$	bMS
2926916965512116864	11.12	11.17	11.05	0.03	$215 \pm 11$	bMS
2927013482021158656	10.74	10.75	10.72	0.00	$70 \pm 9$	bMS
2927208336094874624	11.04	11.07	10.97	0.02	$177 \pm 8$	bMS
2927020663206313472	11.82	11.92	11.63	0.00	$160 \pm 18$	bMS
2926989979960168448	11.18	11.23	11.11	0.01	$122 \pm 12$	bMS
2927018734755286784	11.72	11.82	11.55	0.01	$97 \pm 14$	bMS
2927016574388824064	10.65	10.66	10.63	0.00	$185 \pm 9$	bMS
2927213004717564800	10.50	10.52	10.47	0.04	$252 \pm 7$	rMS
2927008980887462400	10.26	10.28	10.24	0.06	$40 \pm 7$	rMS <sup>b</sup>
2927199849239653760	10.73	10.76	10.68	0.05	$290 \pm 8$	rMS
2927203113414681600	11.00	11.05	10.91	0.06	$290 \pm 8$	rMS
2927022003236076800	11.33	11.39	11.21	0.03	$205 \pm 13$	rMS
2926911223137755136	10.28	10.29	10.27	0.04	$277 \pm 29$	rMS
2926917137310902016	10.60	10.62	10.56	0.04	$252 \pm 7$	rMS
2926994824683234944	10.77	10.81	10.71	0.06	$80 \pm 9$	rMS

Table 1 continued on next page

Table 1 (*continued*)

<i>Gaia</i> ID	<i>G</i> (mag)	<i>G</i> <sub>BP</sub> (mag)	<i>G</i> <sub>RP</sub> (mag)	$\Delta G_{BP} - G_{RP}$	$v \sin i$ (km s <sup>-1</sup> ) <sup>a</sup>	Classification
(1)	(2)	(3)	(4)	(5)	(6)	(7)
2927199746160410496	11.16	11.22	11.06	0.05	247 ± 10	rMS
2927012657387390336	10.26	10.27	10.24	0.05	277 ± 8	rMS
2927008431139550080	11.59	11.70	11.40	0.08	100 ± 12	rMS
2926914182373505152	11.12	11.19	11.02	0.07	220 ± 9	rMS
2926912533106020096	10.86	10.91	10.79	0.06	275 ± 8	rMS
2926916175231589888	11.04	11.09	10.94	0.06	90 ± 8	rMS
2926912361307334528	10.81	10.85	10.75	0.05	232 ± 8	rMS
2927016368239015296	11.25	11.32	11.14	0.05	250 ± 11	rMS
2927013791258742912	9.60	9.59	9.64	0.01	108 ± 6	MSTO
2927209057649389696	9.31	9.29	9.35	0.02	16 ± 12	MSTO <sup>b</sup>
2927213112098494592	9.38	9.36	9.43	0.00	18 ± 11	MSTO <sup>b</sup>
2927010905040796288	8.95	8.95	8.98	0.05	247 ± 5	MSTO
2927005682360625664	8.34	8.33	8.37	0.04	197 ± 5	MSTO
2927203388292592384	9.73	9.72	9.76	0.01	280 ± 5	MSTO
2926993175415844096	9.98	9.97	10.01	0.00	92 ± 7	MSTO
2927009255773305856	9.40	9.41	9.40	0.08	322 ± 6	MSTO
2927012515646285440	7.80	7.78	7.86	0.00 <sup>c</sup>	24 ± 10	MSTO <sup>b</sup>
2927006850591725568	9.06	9.06	9.07	0.07	20 ± 11	MSTO <sup>b</sup>
2927002723118812928	9.36	9.36	9.40	0.03	157 ± 6	MSTO
2927220465082571776	9.15	9.14	9.18	0.04	235 ± 5	MSTO
2927014822050825856	9.16	9.17	9.15	0.11	...	MSTO <sup>b</sup>
2927014100496388736	9.12	9.11	9.14	0.06	270 ± 5	MSTO
2927008396779815808	11.59	11.78	11.27	0.30	155 ± 13	binary
2927004754647430784	10.76	10.85	10.63	0.18	107 ± 10	binary
2927015200007933568	10.39	10.44	10.32	0.13	75 ± 8	binary
2927019529334958848	10.96	11.09	10.77	0.25	18 ± 11	binary <sup>b</sup>
2927007950103249920	11.40	11.56	11.13	0.27	37 ± 12	binary

<sup>a</sup>Uncertainty estimated from the mock test.

<sup>b</sup>Likely a spectroscopic binary.

<sup>c</sup>This star is located at the tip of the blue edge, where the isochrone does not fit well. Thus, the pseudo-color for this star is fixed at 0 mag.

NOTE—(1) *Gaia* DR2 ID; (2, 3, 4) *Gaia* bands; (5) Pseudo-color; (6) Projected rotational velocity; (7) Classification based on CMD.

The  $v \sin i$  values for 53 bright cluster members around the eMSTO, bMS, rMS, and the equal-mass binary sequence span a wide range, from non-rotators to rotation rates greater than 300 km s<sup>-1</sup>. The left panel of Fig. 4 shows the CMD of NGC 2287 with its member stars color-coded by their projected rotational velocities. bMS and rMS stars are well-separated in projected rotational velocity: bMS stars are mainly composed of slow rotators while rMS stars are predominantly rapid rotators. MSTO stars follow a similar trend, with stars getting redder as their rotation rates increase; the cluster's equal-mass binary stars are all slow rotators.

To provide a direct comparison, we overplotted two synthetic, coeval clusters ( $t = 150$  Myr) with different rotational rates ( $\omega = 0$  and  $\omega = 0.8\omega_{\text{crit}}$ ) in the right panel of Fig. 4. The simulation was carried on based on SYCLIST models (Georgy et al. 2013, 2014), assuming a metallicity of  $Z = 0.014$ . The model took into account limb darkening (Claret

2000), and adopted the gravity-darkening law of Espinosa Lara & Rieutord (2011). We also adopted a flat distribution of rotation rates, using single stars only (no binary systems). Realistic photometric uncertainties of 0.003 mag in both  $G$  and  $G_{BP} - G_{RP}$  were added to the simulation. Both the split MS and eMSTO can be well reproduced by these synthetic clusters, favoring a rotation-dominant scenario.

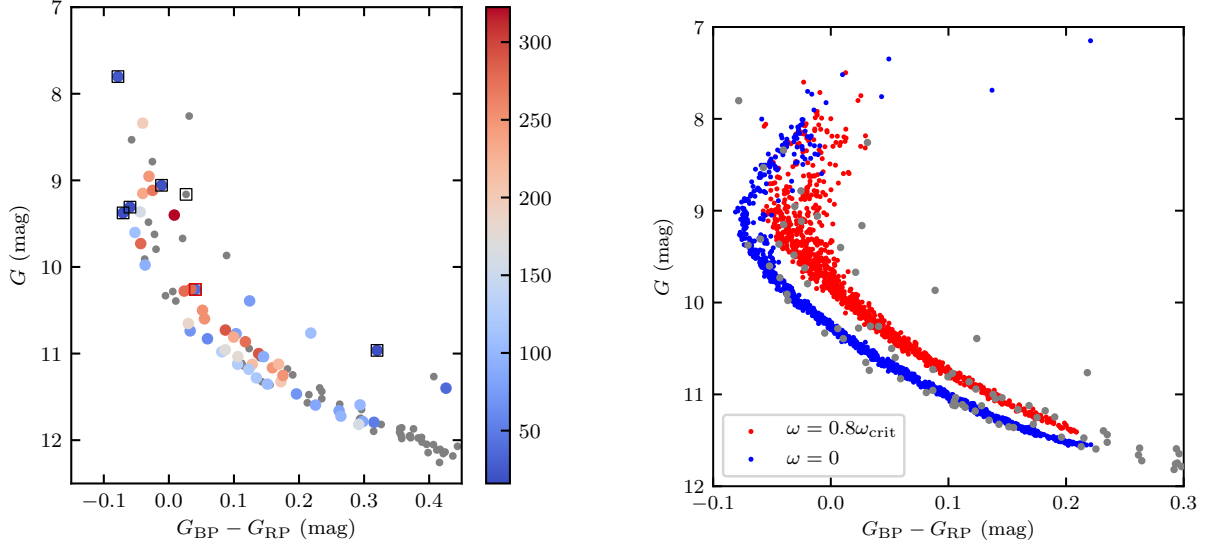


**Figure 4.** (left) CMD of NGC 2287 with stars color-coded according to their projected rotational velocities. Squares represent spectroscopic binaries. *Gaia* ID 2927008980887462400 is indicated by the red square. (right) Synthetic clusters of slowly (blue) and rapidly rotating populations (red;  $\omega = 0.8\omega_{\text{crit}}$ ) at an age of 150 Myr. The expected photometric errors have been added to the simulations.

We now define the pseudo-color  $\Delta G_{BP} - G_{RP}$ , that is, a star’s color difference with respect to the cluster’s blue ridge line, represented by the best-fitting isochrone to the cluster’s dominant stellar population (see Table 1). Fig. 5 shows the distribution of the NGC 2287 split-MS stars in the  $\Delta G_{BP} - G_{RP}$  versus  $v \sin i$  diagram, as well as their respective histograms. The majority of cluster member stars exhibit a clear correlation between  $v \sin i$  and pseudo-color, in the sense that the bMS and rMS populations tend to represent slow and rapid rotational velocities, respectively. The mean projected rotational velocity for bMS stars is  $\langle v \sin i \rangle_{\text{bMS}} = 111 \pm 13 \text{ km s}^{-1}$  ( $\sigma = 46 \text{ km s}^{-1}$ ).

Four rMS stars have projected rotational velocities below  $100 \text{ km s}^{-1}$ ; these coincide with bMS stars in projected velocity space. One of these objects, *Gaia* ID 2927008980887462400 (indicated by the red square in Fig. 4), is a double-lined spectroscopic binary system. It exhibits an additional absorption profile at a wavelength around  $5178 \text{ \AA}$ , which may be related to the presence of a fainter and cooler companion star. Under this assumption and since the primary star’s profile is not significantly affected by the companion, we adopted the projected rotational velocity given by the best-fitting model spectrum as a reliable estimate of the primary star’s rotation rate. This system’s locus on the rMS is therefore determined by its binary nature. The binary’s primary star is expected to be located on the bMS, but it appears redder because of contamination by its unresolved lower-mass (and thus redder) companion. Unresolved binaries will appear brighter and redder than the (single) primary-star MS, thus potentially projecting bMS stars onto the rMS (Li et al. 2013). Three other slowly rotating rMS objects may also be binary systems. Time-domain photometry would be required to ascertain their binary nature.

Except for these four objects, all 11 other rMS stars have rotational velocities well in excess of those characteristic of the bMS stars. The mean projected rotational velocity of rMS stars is then  $\langle v \sin i \rangle_{\text{rMS}} = 255 \pm 10 \text{ km s}^{-1}$  ( $\sigma = 26 \text{ km s}^{-1}$ ). The Spearman coefficient for the correlation between the pseudo-colors and  $v \sin i$  is 0.68 for both the bMS and the rMS ( $p = 2.8 \times 10^{-5}$ ). The cluster’s eMSTO stars show a similar pattern, in the sense that rapidly rotating stars are generally redder than slowly or non-rotating stars. These results strongly suggest that stellar rotation is the underlying physical cause of the split MS and the eMSTO in NGC 2287.

NGC 2287 also exhibits a slightly extended MSTO region (see Fig. 2), which is a common feature of all massive clusters (with masses greater than about  $10^4 M_{\odot}$ ) in the Magellanic Clouds younger than about 3 Gyr and likely

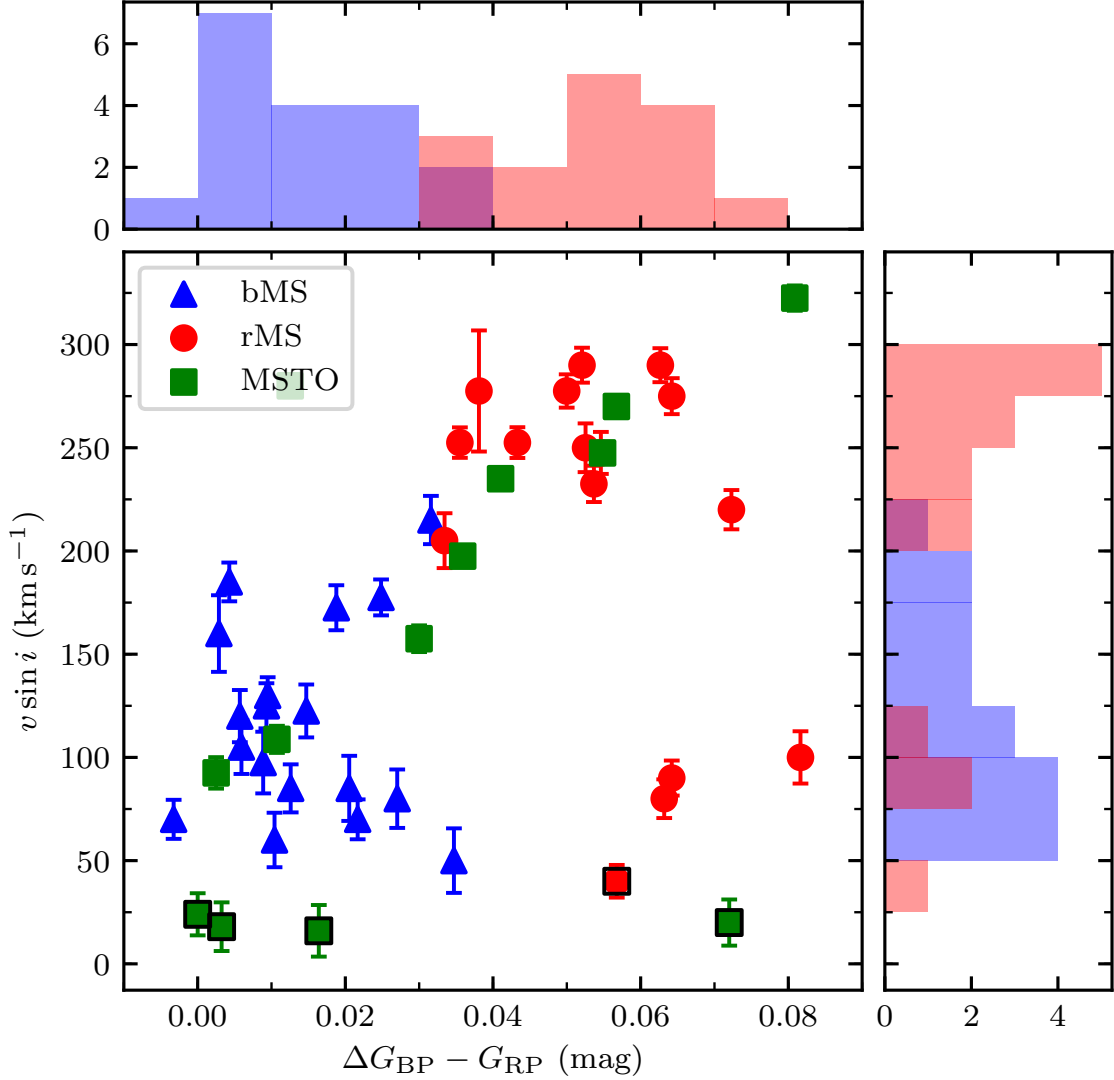


**Figure 5.** Correlation between stellar rotation rates ( $v \sin i$ ) and their CMD loci (represented by pseudo-color,  $\Delta G_{BP} - G_{RP}$ ) for split-MS and MSTO stars. The rMS, bMS, and MSTO stars are represented by red solid circles, blue triangles, and green squares, respectively. The top and right panels show histograms of the pseudo-color and  $v \sin i$  distributions of the bMS and rMS stars, respectively.

caused by stellar rotation (Li et al. 2014). Through analysis of the eMSTO’s morphology, we conclude that the likely effects of stellar rotation in the NGC 2287 CMD may instead be incorrectly interpreted as an age spread spanning  $\sim 100$  Myr. This is consistent with previous studies of massive Magellanic Cloud clusters (Niederhofer et al. 2015) and open clusters in the Milky Way (Cordoni et al. 2018). Note that the split between the bMS and rMS does not extend as far as the eMSTO region. This is mainly owing to the compound effects of gravity darkening and rotational mixing. Whereas gravity darkening associated with rapid rotation causes stars to have apparently lower surface temperatures (von Zeipel 1924), rotational mixing prolongs the stellar MS lifetime (Eggenberger et al. 2010), resulting in bluer colors compared with their slowly rotating counterparts by pulling more fresh hydrogen into the stellar core (Georgy et al. 2013). Girardi et al. (2011) computed evolutionary tracks and isochrones of models with and without rotation. They found that although rapid rotation indeed influences the shape of the evolutionary tracks, isochrones for rapidly rotating stars trace an indistinguishable MSTO locus with respect to their non-rotating counterparts owing to their longer MS lifetimes. This mechanism, which is most prominent around the eMSTO region in NGC 2287 (for stellar

masses  $3 M_{\odot} \leq M \leq 4 M_{\odot}$ ), can offset the effect of gravity darkening, thus explaining the disappearance of the bifurcation towards brighter luminosities.

#### 4. DISCUSSION AND CONCLUSIONS

Numerous studies of young and intermediate-age (1–3 Gyr-old) star clusters have enriched our understanding of stellar rotation in the cluster environment (Dupree et al. 2017; Bastian et al. 2018), and it has become widely acknowledged that stellar rotation plays an important role in changing the morphology of the clusters’ CMDs. One of the remaining questions in this field relates to the actual distribution of equatorial rotational velocities  $v_{\text{eq}}$  and the inclination angle  $i$ . The straightforward assumption that the distribution of stellar rotation axes is stochastic would translate into a uniform three-dimensional orientation distribution. However, a heated dispute as to whether the stellar spin axes in star clusters may be aligned (‘spin alignment’) is currently playing out in the literature. Corsaro et al. (2017) used asteroseismology to measure the inclination angles of the spin axes of 48 red giant stars in two open clusters, NGC 6791 and NGC 6819, and reported strong stellar-spin alignment in both clusters. However, Mosser et al. (2018) instead demonstrated non-alignment of the rotation axes of stars found in these same two clusters. Apart from asteroseismology, several studies have used spectroscopic rotation measurements ( $v \sin i$ ), as well as information pertaining to stellar radii and photometric rotation periods to disentangle the influence of rotational velocity and inclination angle. Jackson & Jeffries (2010) and Jackson et al. (2018) found no evidence of strong alignment in the Pleiades and  $\alpha$  Persei star clusters. However, Kovacs (2018) claimed spin alignment in the Praesepe cluster using similar techniques (but also see Kamiaka et al. 2018, for a critical discussion).

The distribution of projected rotational velocities is an effective tool to constrain the underlying distribution of  $v_{\text{eq}}$  and  $i$  (Lim et al. 2019). Here, we consider three cases. Case 1 adopts a uniform distribution of both  $v_{\text{eq}}$  and orientation in three-dimensional space. Case 2 (spin alignment) is characterized by a uniform distribution of  $v_{\text{eq}}$  and a Gaussian distribution of  $i$ . Case 3 considers a uniform distribution of  $i$  and a bimodal distribution of  $v_{\text{eq}}$  to represent the slowly and rapidly rotating populations,  $v_s$  and  $v_r$ , respectively. The relative numbers of both stellar populations were carefully considered.

In the simulation, the maximum  $v_{\text{eq}}$  was fixed at  $414 \text{ km s}^{-1}$ , corresponding to the maximum  $v_{\text{crit}}$  in our synthetic clusters ( $t = 150 \text{ Myr}$ ). A stochastic orientation in three-dimensional space can be represented by a uniform distribution in  $\cos i$  (Lim et al. 2019). Case 2 has two free parameters to describe its Gaussian profile—the peak inclination angle  $i_{\text{peak}}$  ( $5^\circ$  to  $90^\circ$  in steps of  $5^\circ$ ) and the dispersion  $\sigma_i$  ( $1^\circ$  to  $46^\circ$  in steps of  $5^\circ$ ). For Case 3,  $v_s$  and  $v_r$  range from  $80 \text{ km s}^{-1}$  to  $200 \text{ km s}^{-1}$  and from  $200 \text{ km s}^{-1}$  to  $400 \text{ km s}^{-1}$ , respectively, both in steps of  $20 \text{ km s}^{-1}$ . We confirmed that changing the velocity dispersion did not significantly affect the result, and thus we fixed the velocity dispersion at  $30 \text{ km s}^{-1}$  for convenience. The number fraction of rapid rotators with respect to the entire population ranges from 0.1 to 0.9 in steps of 0.1. For each configuration, we generated 1000 samples and compared them with the observed results using a two-sample Kolmogorov–Smirnov test. To reduce stochastic effects, we repeated this process 1000 times for each configuration and used the median  $p$  value to select which configuration had the highest probability to reproduce the observed distribution.

Fig. 6 shows the cumulative distributions of the projected rotational velocities, as well as the best-fitting simulation results representing Cases 1 to 3. Cases 1 and 2 clearly cannot reproduce the observations (the best-fitting parameters for Case 2 are  $i_{\text{peak}} = 45^\circ$ ;  $\sigma_i = 11^\circ$ ). The best-fitting model of Case 3 ( $p = 0.99$ ; better than Case 2 at the  $3\sigma$  level) yields two rotating populations with peak velocities of  $v_r = 280 \text{ km s}^{-1}$  and  $v_s = 100 \text{ km s}^{-1}$ . This is indeed within  $1\sigma$  of  $\langle v \sin i \rangle_{\text{RMS}}$  and  $\langle v \sin i \rangle_{\text{BMS}}$ . The number ratio of the two populations is  $n_r/n_s = 1$  (see also Fig. 7). This represents the first evidence in support of a dichotomous distribution of real rotational velocities in star clusters. It raises an important question as to the origin of such a bimodal rotational velocity distribution.

In fact, this is not the first time we see such a bimodal rotation distribution. In a census of some 1100 early-type field stars, Royer et al. (2007) found that early-type MS stars show genuine bimodal distributions of true equatorial rotational velocities. Subsequent work by Zorec & Royer (2012) confirmed that stars more massive than  $2.5 M_{\odot}$  exhibit a bimodal equatorial velocity distribution, while less massive stars show a unimodal rotation distribution. However, note that the stellar mass range of the bimodal rotation distribution reported by Zorec & Royer (2012) is not exactly the same as the masses relevant for the split MS and MSTO observed for NGC 2287. The mass of the split MS’s faintest end is estimated at around  $1.7 M_{\odot}$ , which is significantly lower than the dividing mass of the bimodal and unimodal rotation distribution found by Zorec & Royer (2012). Another difference is found in the rotational velocities for the slow and rapid rotators. The peak rotational velocities we derived for NGC 2287 are slightly larger than

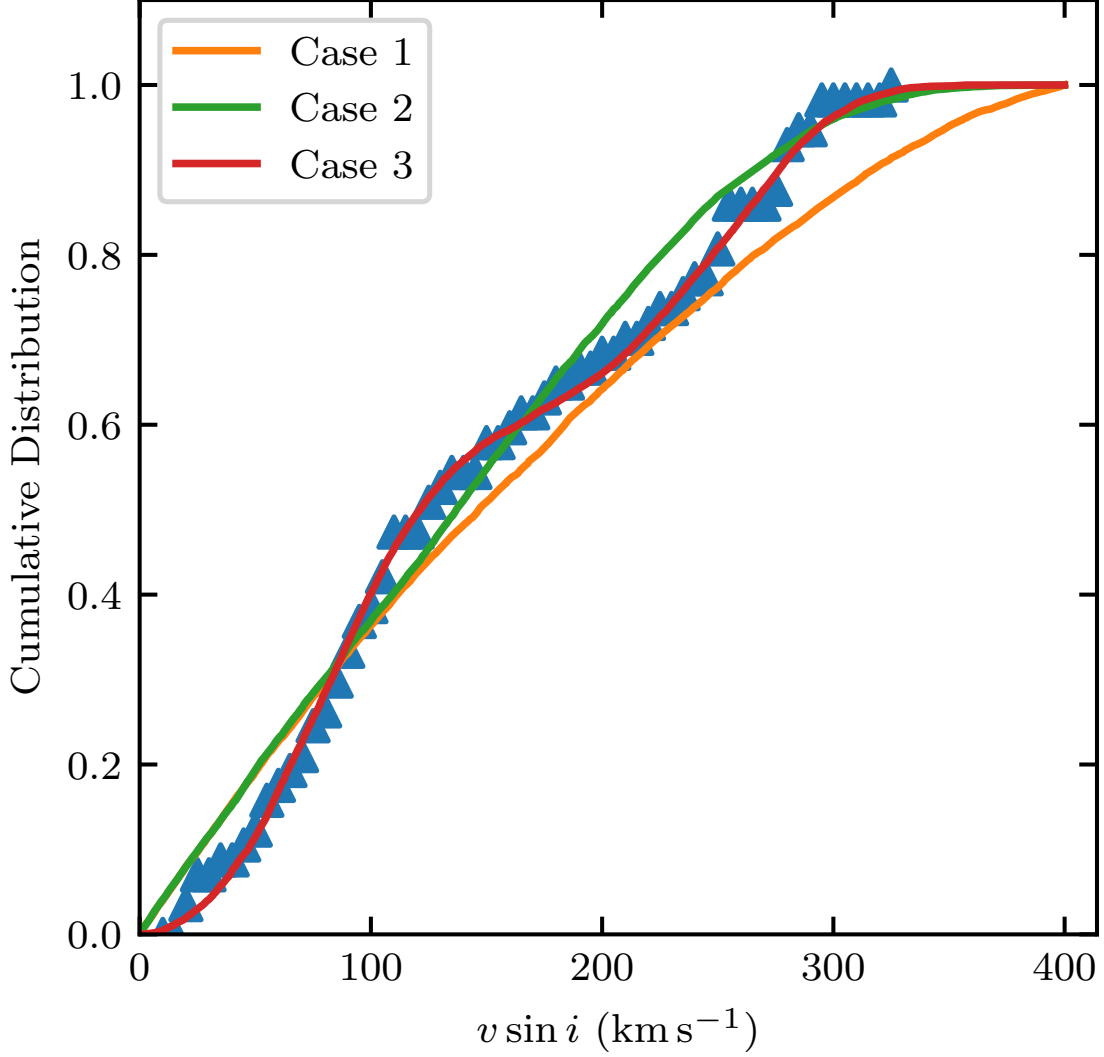


**Figure 6.** Cumulative  $v \sin i$  distribution and best-fitting theoretical models. The observational data are represented by blue triangles. We adopted a maximum  $v_{\text{eq}} = 414 \text{ km s}^{-1}$ . Case 1 (orange): Uniform distributions of both  $v_{\text{eq}}$  and  $i$ . Case 2 (green): Uniform distribution of  $v_{\text{eq}}$ , combined with a Gaussian distribution of  $i$ . Case 3 (red): Bimodal distribution of  $v_{\text{eq}}$ , combined with a uniform distribution of  $i$ .

the values reported by [Zorec & Royer \(2012\)](#) for a similar mass range ( $\sim 40 \text{ km s}^{-1}$  and  $\sim 210 \text{ km s}^{-1}$  for slow and fast rotators, respectively). These disagreements remain even if we consider the effects associated with the different evolutionary MS phases for different masses.

[Zorec & Royer \(2012\)](#) argued that in late A-type stars ( $1.6 M_{\odot} \leq M \leq 2.5 M_{\odot}$ ), rotational velocities are accelerated during the first one-third of their MS lifetime and then remain high for a long time, while massive stars ( $2.5 M_{\odot} \leq M \leq 3.5 M_{\odot}$ ) undergo efficient deceleration up to the terminal MS age. However, essential evidence is still lacking to account for the high fraction of slow rotators in the high-mass regime and vice versa. These conditions are unable to explain our observations of NGC 2287. [Zorec & Royer \(2012\)](#) suggested that tidal braking by close binaries could be at work. In fact, [D’Antona et al. \(2017\)](#) argued that the bMS in young clusters might be the outcome of fast braking of the rapidly rotating population. Magnetic-wind braking or tidal torques owing to a binary companion can, in theory, rapidly decelerate a star’s rotation rate (that is, over a short period compared with the cluster’s age) and transfer the star’s evolution from the rapidly rotating to the non-rotating track. Meanwhile, the core hydrogen content would remain unchanged, thus making the cluster appear younger in the CMD. Here, we explore whether the bMS stars in

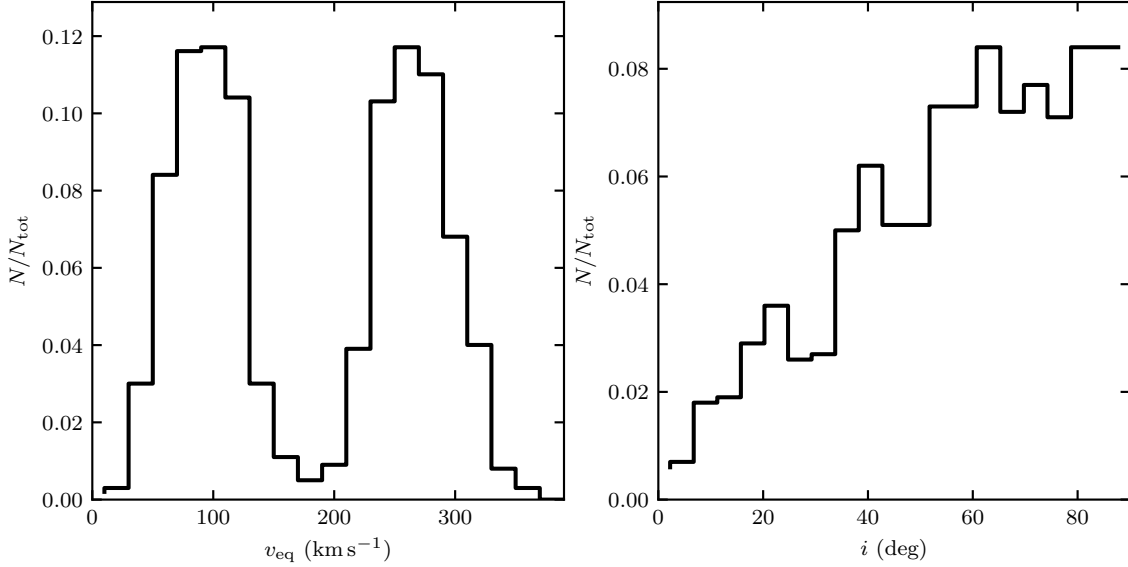


**Figure 7.** Example of best-fitting  $v_{\text{eq}}$  and  $i$  distributions for Case 3. The bimodal distribution of velocities peaks at both  $100 \text{ km s}^{-1}$  and  $280 \text{ km s}^{-1}$ . The velocity dispersion is  $30 \text{ km s}^{-1}$  and the number ratio of the slowly and rapidly rotating populations is unity.

NGC 2287 could be composed of a population of slow rotators ( $\sim 100 \text{ km s}^{-1}$ ) which may have slowed down from their initial state of rapid rotation by low-mass-ratio ( $q \leq 0.4$ ) binary companions.

We adopted  $2 M_{\odot}$  and  $2 R_{\odot}$  as, respectively, the typical mass and radius of the bMS population and estimated the synchronization timescale for such a star with a radiative envelope (Hurley et al. 2002),

$$\frac{1}{\tau_{\text{sync}}} = 52^{5/3} \left( \frac{GM}{R^3} \right)^{1/2} \frac{MR^2}{I} q_2^2 (1 + q_2)^{5/6} E_2 \left( \frac{R}{a} \right)^{17/2}, \quad (1)$$

where  $G$  is the gravitational constant,  $M$  and  $R$  the stellar mass and radius, respectively,  $q_2$  the mass ratio,  $I$  the moment of inertia and  $E_2$  is a second-order tidal coefficient which can be fitted to values given by Zahn (1975), i.e.,

$$E_2 = 1.592 \times 10^{-9} M^{2.84}. \quad (2)$$

In Fig. 8, we display the synchronization timescale for various mass ratios  $q$  and binary separations  $a$  for a  $2.0 M_{\odot}$  star. The synchronization timescale of a close binary system ( $a \leq 7 R_{\odot}$ ) is relatively short compared with the age of NGC 2287. We also overplotted the expected relation between  $a$  and  $q$  for slow rotators, calculated using Kepler's Third Law, assuming that the binary system is already tidally locked and the orbital and rotational periods are the same. The corresponding orbital period is around  $P = 1$  day for  $v_{\text{eq}} = 100 \text{ km s}^{-1}$  ( $\sigma = 30 \text{ km s}^{-1}$ ). The region in the  $a$  versus  $q$  diagram where such stars may be found overlaps with the synchronization timescale mainly between 1.5 Myr and 15 Myr.

The colors of higher-mass-ratio ( $q \geq 0.5$ ) unresolved binaries will be reddened significantly compared with those of their lower-mass-ratio counterparts. Unresolved higher-mass-ratio binary systems will therefore appear on the rMS rather than the bMS. Tidal locking, that is, the synchronization of the primary and secondary stellar rotation rates can effectively drain a system's angular momentum into the orbital system (de Mink et al. 2013). The synchronization timescale (Hurley et al. 2002) for a typical bMS star in a close binary system is, in general, much shorter than the host cluster's age, particularly so for NGC 2287 (see Fig. 8). By the time the cluster has evolved to its current age, such close binary systems will have become locked through tidal interactions, thus forming a population of slow rotators segregated in color from rapid rotators. Assuming that the binary system is tidally locked and the orbital period ( $a$ ) is the same as the rotational period, the expected relation between  $a$  and  $q$  for slow rotators also supports the notion that such binary systems are likely to decelerate the stellar rotation rates and, thus, become a bMS population as observed.

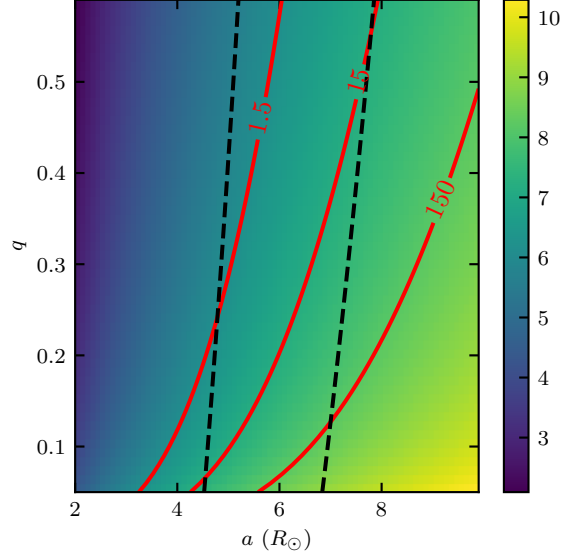


**Figure 8.** Synchronization timescale of a  $2M_{\odot}$  primary star for various mass ratios ( $q$ ) and binary separations ( $a$ ). The color represents the synchronization timescale (in logarithmic units, yr). The three contour lines represent 1.5 Myr, 15 Myr and 150 Myr (1%, 10%, and 100% of the cluster’s age). The black dashed lines enclose the expected relation between  $a$  and  $q$  for slow rotators if we assume that our binary systems are already tidally locked and the orbital and rotational periods are identical.

The scenario advocated by D’Antona et al. (2017) cannot be ruled out. However, the bMS-to-rMS number ratio of near unity we have found in NGC 2287 is hard to explain on this basis. (Moe & Di Stefano 2017) found that, unlike the situation for solar-type stars, which are characterized by a log-normal orbital-period distribution with a peak near  $\log P \approx 5$  [days], O- and early-B type stars show a bimodal distribution with peaks at short ( $\log P \leq 1$  [days]) and intermediate ( $\log P \approx 3.5$  [days]) periods. As the primary mass increases, the fraction of rapidly orbiting binaries increases and could be comparable to or even higher than the fraction of binaries with longer orbital periods. However, the fraction of short orbital period binaries becomes significant only for masses in excess of  $9M_{\odot}$ . Although the reasons are still unclear, this may be associated with some mechanism driving the orbital evolution which causes the companion to migrate inwards, to the inside of the circumstellar disk. However, the bMS-to-rMS number ratio we have found for NGC 2287 does not fit easily in this pattern. In addition, its mass ratio distribution is also peculiar. A few systems are located perfectly on the equal-mass binary sequence, implying that they have mass ratios close to unity. Our observational evidence shows that in NGC 2287, binary systems have either very low or very high (near unity) mass ratios, since no objects with intermediate mass ratios appear to be present in the CMD.

Our results imply that the clearly separated double MSs in NGC 2287 can result from a random distribution of inclination angles and a dichotomous distribution of equatorial rotational velocities with peaks near  $100 \text{ km s}^{-1}$  and  $280 \text{ km s}^{-1}$ . The slow rotators are likely stars that initially rotated rapidly but subsequently slowed down through tidal locking induced by low-mass-ratio binary systems. The short tidal-braking timescale characteristic of these bMS stars ( $\leq 10\%$  of the cluster’s age) thus renders the distribution of rotational velocities dichotomous. However, the cluster would have a much larger population of short period binaries than is seen in the literature, with relatively low secondary masses. Although still speculative, future time-domain observations of bMS stars may shed additional light on the underlying physical processes.

R. d. G. and L. D. acknowledge research support from the National Natural Science Foundation of China through grants 11633005, 11473037, and U1631102. C. L. and L. D. are grateful for support from the National Key Research and Development Program of China through grant 2013CB834900 from the Chinese Ministry of Science and Technology. This work has made use of data from the European Space Agency (ESA) mission *Gaia* (<https://www.cosmos.esa.int/gaia>), processed by the *Gaia* Data Processing and Analysis Consortium (DPAC, <https://www.cosmos.esa.int/web/gaia/dpac/consortium>). Funding for the DPAC has been provided by national institutions, in particular the

institutions participating in the *Gaia* Multilateral Agreement. Also based on observations made with ESO Telescopes at the La Silla Paranal Observatory under programme ID 380.D-0161.

*Software:* PARSEC (1.2S; [Bressan et al. 2012](#)), Astropy ([Astropy Collaboration et al. 2013](#)), Matplotlib ([Hunter 2007](#)), SYNSPEC ([Hubeny & Lanz 1992](#))

## REFERENCES

- Andrae, R., Fouesneau, M., Creevey, O., et al. 2018, *A&A*, 616, A8
- Astropy Collaboration, Robitaille, T. P., Tollerud, E. J., et al. 2013, *A&A*, 558, A33
- Bastian, N., Cabrera-Ziri, I., Niederhofer, F., et al. 2017, *MNRAS*, 465, 4795
- Bastian, N., Kamann, S., Cabrera-Ziri, I., et al. 2018, *MNRAS*, 480, 3739
- Bastian, N., & Lardo, C. 2018, *A&A Rv*, 56, 83
- Brandt, T. D., & Huang, C. X. 2015aa, *ApJ*, 807, 25
- Brandt, T. D., & Huang, C. X. 2015bb, *ApJ*, 807, 24
- Brandt, T. D., & Huang, C. X. 2015cc, *ApJ*, 807, 58
- Bressan, A., Marigo, P., Girardi, L., et al. 2012, *MNRAS*, 427, 127
- Cardelli, J. A., Clayton, G. C., & Mathis, J. S. 1989, *ApJ*, 345, 245
- Claret, A. 2000, *A&A*, 359, 289
- Cordoni, G., Milone, A. P., Marino, A. F., et al. 2018, *ApJ*, 869, 139
- Correnti, M., Goudfrooij, P., Bellini, A., et al. 2017, *MNRAS*, 467, 3628
- Corsaro, E., Lee, Y.-N., García, R. A., et al. 2017, *Nat. Astron.*, 1, 64
- D’Antona, F., Di Criscienzo, M., Decressin, T., et al. 2015, *MNRAS*, 453, 2637
- D’Antona, F., Milone, A. P., Tailo, M., et al. 2017, *Nat. Astron.*, 1, 186
- de Mink, S. E., Langer, N., Izzard, R. G., et al. 2013, *ApJ*, 764, 166
- Dupree, A. K., Dotter, A., Johnson, C. I., et al. 2017, *ApJL*, 846, L1
- Eggenberger, P., Miglio, A., Montalbán, J., et al. 2010, *A&A*, 509, A72
- Espinosa Lara, F., & Rieutord, M. 2011, *A&A*, 533, A43
- Gaia Collaboration, Brown, A. G. A., Vallenari, A., et al. 2016, *A&A*, 595, A2
- Gaia Collaboration, Brown, A. G. A., Vallenari, A., et al. 2018, *A&A*, 616, A1
- Georgy, C., Ekström, S., Granada, A., et al. 2013, *A&A*, 553, A24
- Georgy, C., Granada, A., Ekström, S., et al. 2014, *A&A*, 566, A21
- Girardi, L., Eggenberger, P., & Miglio, A. 2011, *MNRAS*, 412, L103
- Goudfrooij, P., Puzia, T. H., Kozhurina-Platais, V., et al. 2011, *ApJ*, 737, 3
- Huang, W., & Gies, D. R. 2006, *ApJ*, 648, 580
- Huang, W., Gies, D. R., & McSwain, M. V. 2010, *ApJ*, 722, 605
- Hubeny, I., & Lanz, T. 1992, *A&A*, 262, 501
- Hunter, J. D. 2007, *Comput. Sci. Eng.*, 9, 90
- Hurley, J. R., Tout, C. A., & Pols, O. R. 2002, *MNRAS*, 329, 897
- Jackson, R. J., Deliyannis, C. P., & Jeffries, R. D. 2018, *MNRAS*, 476, 3245
- Jackson, R. J., & Jeffries, R. D. 2010, *MNRAS*, 402, 1380
- Kamiaka, S., Benomar, O., & Suto, Y. 2018, *MNRAS*, 479, 391
- Kharchenko, N. V., Piskunov, A. E., Röser, S., et al. 2005, *A&A*, 438, 1163
- Kovacs, G. 2018, *A&A*, 612, L2
- Kurucz, R. L. 2005, *Mem. Soc. Astron. It. Suppl.*, 8, 189
- Li, C., de Grijs, R., & Deng, L. 2013, *MNRAS*, 436, 1497
- Li, C., de Grijs, R., & Deng, L. 2014, *Nature*, 516, 367
- Li, C., de Grijs, R., Deng, L., et al. 2017, *ApJ*, 844, 119
- Lim, B., Rauw, G., Nazé, Y., et al. 2019, *Nat. Astron.*, 3, 76
- Mackey, A. D., Broby Nielsen, P., Ferguson, A. M. N., et al. 2008, *ApJL*, 681, L17
- Marino, A. F., Milone, A. P., Casagrande, L., et al. 2018a, *ApJL*, 863, L33
- Marino, A. F., Przybilla, N., Milone, A. P., et al. 2018b, *AJ*, 156, 116
- Milone, A. P., Bedin, L. R., Cassisi, S., et al. 2013, *A&A*, 555, A143
- Milone, A. P., Bedin, L. R., Piotto, G., et al. 2009, *A&A*, 497, 755
- Milone, A. P., Bedin, L. R., Piotto, G., et al. 2015, *MNRAS*, 450, 3750
- Milone, A. P., Marino, A. F., D’Antona, F., et al. 2016, *MNRAS*, 458, 4368
- Milone, A. P., Marino, A. F., D’Antona, F., et al. 2017, *MNRAS*, 465, 4363
- Milone, A. P., Marino, A. F., Di Criscienzo, M., et al. 2018, *MNRAS*, 477, 2640

- Moe, M., & Di Stefano, R. 2017, *ApJS*, 230, 15
- Mosser, B., Gehan, C., Belkacem, K., et al. 2018, *A&A*, 618, A109
- Niederhofer, F., Georgy, C., Bastian, N., et al. 2015, *MNRAS*, 453, 2070
- O'Donnell, J. E. 1994, *ApJ*, 422, 158
- Palacios, A., Gebran, M., Josselin, E., et al. 2010, *A&A*, 516, A13
- Pasquini, L., Avila, G., Blecha, A., et al. 2002, *Msngr*, 110, 1
- Platais, I., Melo, C., Quinn, S. N., et al. 2012, *ApJL*, 751, L8
- Rivinius, T., Carciofi, A. C., & Martayan, C. 2013, *A&A Rv*, 21, 69
- Royer, F., Zorec, J., & Gómez, A. E. 2007, *A&A*, 463, 671
- Sun, W., de Grijs, R., Deng, L., et al. 2019, *ApJ*, 876, 113
- von Zeipel, H. 1924, *MNRAS*, 84, 665
- Zahn, J.-P. 1975, *A&A*, 41, 329
- Zorec, J., & Royer, F. 2012, *A&A*, 537, A120